

Northumbria Research Link

Citation: Giannakis, Iraklis, Zhou, Feng, Warren, Craig and Giannopoulos, Antonios (2021) Inferring the Shallow Layered Structure at the Chang'E-4 Landing Site: A Novel Interpretation Approach Using Lunar Penetrating Radar. *Geophysical Research Letters*, 48 (16). e2021GL092866. ISSN 0094-8276

Published by: American Geophysical Union

URL: <https://doi.org/10.1029/2021gl092866> <<https://doi.org/10.1029/2021gl092866>>

This version was downloaded from Northumbria Research Link:
<http://nrl.northumbria.ac.uk/id/eprint/46652/>

Northumbria University has developed Northumbria Research Link (NRL) to enable users to access the University's research output. Copyright © and moral rights for items on NRL are retained by the individual author(s) and/or other copyright owners. Single copies of full items can be reproduced, displayed or performed, and given to third parties in any format or medium for personal research or study, educational, or not-for-profit purposes without prior permission or charge, provided the authors, title and full bibliographic details are given, as well as a hyperlink and/or URL to the original metadata page. The content must not be changed in any way. Full items must not be sold commercially in any format or medium without formal permission of the copyright holder. The full policy is available online: <http://nrl.northumbria.ac.uk/policies.html>

This document may differ from the final, published version of the research and has been made available online in accordance with publisher policies. To read and/or cite from the published version of the research, please visit the publisher's website (a subscription may be required.)

Geophysical Research Letters

RESEARCH LETTER

10.1029/2021GL092866

Key Points:

- We suggest a novel hyperbola-fitting technique that assumes an arbitrary permittivity distribution with respect to depth
- The proposed method is used to map the lunar regolith at the Chang'E-4 landing site
- A layered structure is revealed at the first 10 meters. A new stratigraphic model is suggested for the Von Kármán crater

Supporting Information:

Supporting Information may be found in the online version of this article.

Correspondence to:

I. Giannakis,
iraklis.giannakis@abdn.ac.uk

Citation:

Giannakis, I., Zhou, F., Warren, C., & Giannopoulos, A. (2021). Inferring the shallow layered structure at the Chang'E-4 landing site: A novel interpretation approach using lunar penetrating radar. *Geophysical Research Letters*, 48, e2021GL092866. <https://doi.org/10.1029/2021GL092866>

Received 5 FEB 2021
Accepted 9 JUL 2021

Inferring the Shallow Layered Structure at the Chang'E-4 Landing Site: A Novel Interpretation Approach Using Lunar Penetrating Radar

Iraklis Giannakis¹ , Feng Zhou² , Craig Warren³ , and Antonios Giannopoulos⁴ 

¹School of Geosciences, University of Aberdeen, Kings College, Aberdeen, UK, ²School of Mechanical Engineering and Electronic Information, China University of Geosciences (Wuhan), Wuhan, China, ³Department of Mechanical and Construction Engineering, Northumbria University, Newcastle, UK, ⁴School of Engineering, The University of Edinburgh, Edinburgh, UK

Abstract The current paper investigates the shallow layers of the lunar regolith at the Chang'E-4 landing site. Four layers between 0 and 10 m were identified using lunar penetrating radar. Based on these outputs, a revised stratigraphic model is suggested for the post-Imbrian ejecta at the Von Kármán crater. The layers were previously unseen due to the smooth boundaries between them. The revised model was inferred using an advanced hyperbola-fitting scheme. Applying conventional hyperbola-fitting to non-homogeneous media results in errors and inaccuracies that are often wrongly assumed to be negligible. We propose a novel hyperbola-fitting scheme that is, not constrained to homogeneous media and can be applied subject to any arbitrary one-dimensional permittivity distribution. Via this approach, we can estimate the permittivity profile of an investigated area and detect layered structures that were previously transparent to electromagnetic waves due to the gradational dielectric properties at their interfaces.

Plain Language Summary The landing site of Chang'E-4 is at the Von Kármán (VK) crater at the South Pole-Aitken (SPA) basin. The SPA basin is the oldest and biggest basin on the Moon created at the early stages of its evolution by an impact that is, believed to have penetrated the lunar crust and uplifted materials from the top mantle. Understanding the geology and stratigraphy of the SPA basin can help us understand cratering processes and shed light on the evolution of the Moon. To that extent, ground penetrating radar (GPR) has been added to the payload of Yutu-2 to investigate the stratigraphy of the Chang'E-4 landing site. One drawback of GPR is that conventional processing methods fail to detect layers with smooth boundaries between them. Consequently, GPR data might give the false impression that an area is relatively homogenous, while in fact it might consist of numerous gradational layers representing a much more complex geological history. In the current paper, a novel interpretation tool is described, capable of detecting smooth transitions between layers. The proposed methodology revealed a previously unseen layered structure for the first ~10 m of the VK crater.

1. Introduction

Ground penetrating radar (GPR) is a mature geophysical technique (Daniels, 2004) with a unique span of applications ranging from landmine detection (Feng et al., 2012; Giannakis et al., 2016) and concrete inspection (Giannakis et al., 2020; Wai-Lok Lai et al., 2018), to glaciology (Williams et al., 2014) and archeology (Conyers, 2004). In planetary sciences, GPR has been applied both for satellite (Lauro et al., 2020) and in-situ measurements (Li et al., 2020), with promising results for mapping sub-glacial water bodies in Mars (Lauro et al., 2020), and for inferring the layered structure of the lunar regolith (Lai et al., 2020; Li et al., 2020; Zhang et al., 2020).

Subject to the application and the employed measurement configuration, various GPR processing and interpretation techniques have been suggested over the years (Daniels, 2004). From typical signal processing (Cassidy, 2009; Li et al., 2015) linear Born approximations (Boero et al., 2018) and machine learning (Giannakis et al., 2019) to full-waveform inversion (Meles et al., 2010). Within that context, hyperbola-fitting is considered one of the most mainstream techniques for the interpretation of common-offset GPR data (Mertens et al., 2016). The simplicity and computational efficiency of hyperbola-fitting make it an appealing

choice for mapping the dielectric properties of an investigated medium, and for estimating the coordinates of subsurface targets (Mertens et al., 2016).

Hyperbola-fitting has been used in both Chang'E-3 and Chang'E-4 missions (Dong, Feng, Zhao, et al., 2020; Dong, Feng, Zhou, et al., 2020; Fa, 2020; Lai et al., 2019; Li et al., 2020) for estimating the electric permittivity of the lunar regolith and subsequently inferring its density and mineralogical composition (Dong, Feng, Zhou, et al., 2020; Li et al., 2020). Nonetheless, the underlying assumptions of hyperbola-fitting constrain its applicability, especially in complex environments where permittivity varies with depth. To mitigate that, conventional hyperbola-fitting is often complemented with the Dix conversion (Dix, 1955; Dong, Feng, Zhao, et al., 2020) in order to transform the estimated bulk velocity to actual velocity. Through a series of numerical examples presented in this paper, it is illustrated that the conventional approach (Dong, Feng, Zhao, et al., 2020) has limited applicability for the lunar regolith and should be used with caution. To that extent, we present a novel hyperbola-fitting that tackles this problem by simultaneously fitting multiple hyperbolas subject to any arbitrary 1D permittivity distribution.

The proposed scheme is applied to the lunar penetrating radar (LPR) data collected by the Yutu-2 rover during the first two lunar days of the Chang'E-4 mission at the Von Kármán (VK) crater (Li et al., 2020). Four distinct layers—that were previously not visible due to the smooth boundaries between them—were identified within the first 10 m. This outcome differs significantly from previous theories suggesting that the first 12 m of the landing site are fairly homogeneous, part of the weathered fine-grained regolith that lies on top of the ejecta from the Finsen crater (Zhang et al., 2020). Based on the revised permittivity profile and the available literature on the geology of the Chang'E-4 landing site, we suggest a new post-Imbrian stratigraphic model for the VK crater, in which an approximately ~ 3 m weathered fine-grained layer is followed by ~ 8 m of ejecta from the VK L and L' craters overlying the ejecta from the Finsen crater.

2. Methodology

2.1. Advanced Hyperbola-Fitting

In this section, a novel hyperbola-fitting framework is described, capable of dealing with half-spaces with arbitrary 1D relative permittivity distributions $\epsilon(y)$ (see Figure S1). A detailed description of conventional hyperbola fitting using the Dix convention is given in Text S1. Similar to typical hyperbola-fitting, in order to avoid non-uniqueness (Giannakis et al., 2019; Mertens et al., 2016), the proposed scheme assumes that the radius (R) of the investigated target equals zero. Subject to a varying velocity with depth, the two way travel time t that it takes for the wave to travel from the point $\vec{B} = \langle x, y \rangle$ to the point $\vec{A} = \langle x_0, d \rangle$ via the parametric curve $\vec{q}(m) = \langle q_x(m), q_y(m) \rangle$ (where $m \in [0 - 1]$ and d is the depth of the target) can be calculated using a scalar line integral over $\vec{q}(m)$

$$t = \frac{2}{c_0} \int_0^1 \sqrt{\epsilon(y)} \left\| \frac{\partial \vec{q}(m)}{\partial m} \right\| dm. \quad (1)$$

Given a specific velocity structure, the path $\vec{q}(m)$ can be calculated using Fermat's principle (Aldo, 1996). The notation $\frac{\partial \vec{q}(m)}{\partial m}$ is used to denote the norm of the first derivative of the parametric curve $\vec{q}(m)$ with respect to the parameter $m \in [0 - 1]$. It is shown that if we simplify Equation 1 and make the assumption that the path $\vec{q}(m)$ is the straight line that connects the antenna to the center of the target, it leads to an elegant and computationally efficient formulation without compromising accuracy (more details are given in Section 2.2). The straight line that connects the antenna to the target can be expressed via the parametric curve $\vec{q}(m) = \vec{A} + (\vec{B} - \vec{A})m$. Substituting this into Equation 1 results in

$$t = \frac{2 \|\vec{B} - \vec{A}\|}{c_0} \int_0^1 \sqrt{\epsilon(y)} dm. \quad (2)$$

The linear path of the integral in Equation 2 can be written as $\vec{q}(m) = \langle x_i + m(x_0 - x_i), y_i + m(d - y_i) \rangle$, where x_i, y_i are the coordinates of the antenna at the i th position. Consequently, the y variable in Equation 2 can be substituted by $y = y_i + m(d - y_i)$, which implies that, for $y_i = 0$ (antenna placed at the surface) $\frac{\partial y}{\partial m} = d$ and that $y = d$ for $m = 1$. Therefore, Equation 2 can be re-written as

$$t = \frac{2 \|\vec{B} - \vec{A}\|}{c_0 d} \int_0^d \sqrt{\epsilon(y)} dy. \quad (3)$$

Solving the integral numerically yields

$$t \approx \frac{2 \|\vec{B} - \vec{A}\|}{c_0 d} \sum_{s=0}^Q \sqrt{\epsilon(s \cdot \Delta y)} \Delta y \quad (4)$$

where Δy is the discretization step and $Q = d / \Delta y$. Notice that the summation term $N(d, \epsilon) = \sum_{s=0}^Q \sqrt{\epsilon(s \cdot \Delta y)} \Delta y$ is independent of the position of the antenna and needs to be calculated just once. The final formulation for the proposed scheme is given by

$$t \approx \frac{2 \|\vec{B} - \vec{A}\|}{c_0 d} N(d, \epsilon), \quad (5)$$

where the only unknowns are the relative permittivity function $\epsilon(y)$ and the depth of the target d . The parameter x_0 can be easily derived from the apex of the hyperbola at the measured B-Scan. Subject to a given $\epsilon(y)$, the depth of the target is calculated using the apex of the hyperbola (x_0, t_0) , where $\|\vec{B} - \vec{A}\| = d$

$$t_0 \approx \frac{2}{c_0} N(d, \epsilon). \quad (6)$$

For a given $\epsilon(y)$, the only unknown in Equation 6 is the depth d that is, estimated numerically using the bisection method. Notice that both Equation 6 and the summation $N(d, \epsilon)$ in Equation 4 need to be evaluated just once. The only term in Equation 5 that needs to be updated as the scan progresses is the distance $\|\vec{B} - \vec{A}\|$. To summarize, given a permittivity distribution $\epsilon(y)$ and the apex of a hyperbola (x_0, t_0) , the depth d of the target is estimated by numerically solving Equation 6 using the bisection method. Subsequently, $N(d, \epsilon)$ is evaluated and furthermore used in Equation 5 to calculate the arrival times.

The proposed scheme utilizes numerous hyperbolas and tries to find the optimum $\epsilon(y)$ that simultaneously minimizes $\min_{\epsilon(y)} \sum_{i=1}^Z \|\mathbf{t}_i - \mathbf{T}_i\|$, where $\mathbf{T}_i \in \mathbb{R}^{n_i}$ and $\mathbf{t}_i \in \mathbb{R}^{n_i}$ represent the measured and predicted arrival times for the i th hyperbola, Z is the total number of the employed hyperbolas and n_i is the number of discretization points for the i th hyperbola. To further simplify the problem, the permittivity is discretized with K equidistant points and subsequently a cubic interpolation is applied to map ϵ with respect to y in a continuous manner. Therefore, the minimization is re-written as $\min_{\epsilon^{(k)} \in \mathbb{R}^K} \sum_{i=1}^Z \|\mathbf{t}_i - \mathbf{T}_i\|$ with only K unknowns. This is a non-linear and non-convex problem that can be solved using global optimizers. A Particle Swarm Optimisation (PSO) (Kennedy & Eberhart, 1995), with 50 particles and uniform PSO parameters, was proven to be very efficient for reconstructing $\epsilon(y)$, given a sufficient number of measured hyperbolas. The number of equidistant points K is estimated by plotting the Error- K curve. This approach is based on the L-curve method (Hansen, 1992) that tries to balance accuracy and constraints. Within that context, we choose the K value for which the solution balances accuracy and simplicity. In particular, the minimization is executed multiple times with increasing K until the error starts to converge. The K value is chosen at the earliest point of convergence. Greater K values can potentially result (if a sufficient number of hyperbolas is not present) in unnecessary complicated permittivity structures without increasing the fitting accuracy.

2.2. Numerical Experiments

Two numerical 2D case studies (illustrated in Figure 1a) are used in this section to evaluate the performance of the proposed scheme. Both models are non-dispersive, non-conductive, and non-magnetic, with a varying relative permittivity with respect to depth $\epsilon(y)$. In both scenarios, the relative permittivity varies with respect to depth and ranges from 2 to 10. Nine perfect electric conductors are distributed randomly within a $2 \times 1 \text{ m}^2$ domain. The targets have a cylindrical shape with 5 cm diameter and their main axis is perpendicular to the acquisition line. Measurements are taken every 2 cm along the x -axis using a line source with 1 GHz central frequency. The offset between the transmitter and the receiver is 1 cm. The numerical simulations were executed using gprMax (Warren et al., 2016, 2019), an open source electromagnetic solver that uses a second order (in both space and time) finite-difference time domain (FDTD) method (Yee, 1966). The spatial discretization step of the FDTD grid is $\Delta x = \Delta y = 5 \text{ mm}$, and the time step Δt is calculated using the

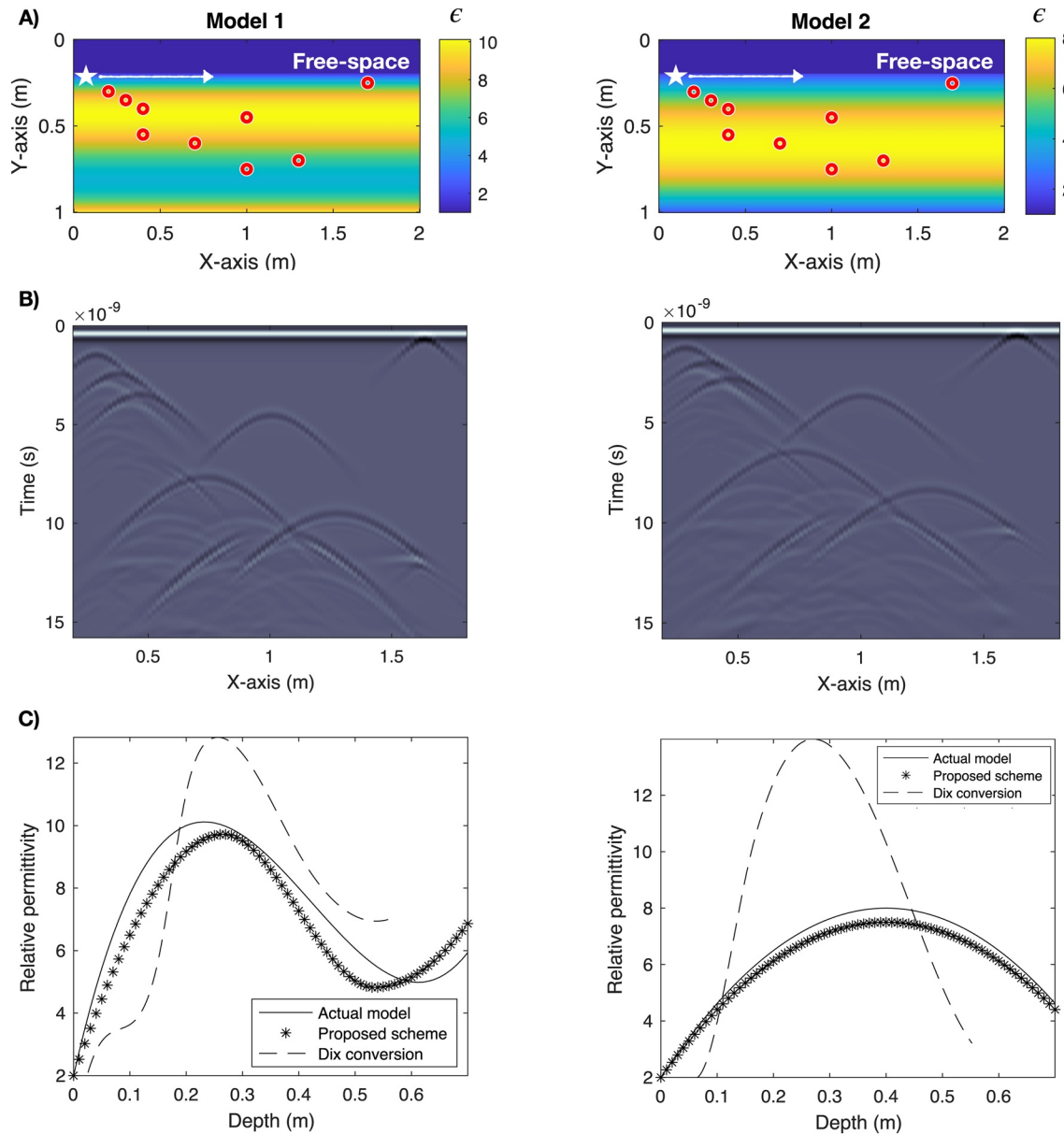


Figure 1. (a) The investigated numerical experiments. Nine cylindrical targets are buried in two media with varying permittivity with respect to depth. Measurements are taken every 2 cm (from left to right) using a ground-coupled line source (white star) with 1 GHz central frequency. (b) Resulting B-Scans. It is evident that due to the smooth boundaries between the layers, no reflections are visible on the resulting radargrams. The shapes of the hyperbolas are the only features that can be used to infer the permittivity profile. (c) The resulting permittivity profile for the models shown in panel (a).

Courant limit (Tafløve & Hagness, 2000). The boundaries of the domain are truncated using the recursive integration perfectly matched layer (Giannopoulos, 2008). The gprMax input files used to generate both models are given in Texts S2 and S3.

The results are shown in Figure 1b where most of the hyperbolas (and their multiples) are clearly visible, as expected in this clutter-free environment. From Figure 1b, it is apparent that even in these clinical clutter-free numerical experiments, the reflections from the layers are very weak and not visible in the measured radargrams. This is due to the smooth transition between the layers that can greatly decrease their reflection coefficient (Bano, 2006; Diamanti et al., 2014). This gives the false impression that a medium is homogeneous when in fact it can be as complex as the investigated case studies (see Figure 1a), with four clear and distinct layers. This is very important when interpreting radargrams from the lunar regolith,

where smooth transitions between layers are expected due to impact gardening and the reworking of the materials during crater formation (Ding et al., 2020). The term “impact gardening” used throughout the paper refers to the alteration of lunar surface due to the gradual gardening of lunar materials via small meteorite impacts (Horz et al., 1991; Pieters & Noble, 2016).

The proposed scheme and the typical hyperbola-fitting with Dix conversion (Dong, Feng, Zhao, et al., 2020) (see Text S1) were applied to the radargrams shown in Figure 1b. In both models, the proposed methodology outperforms conventional hyperbola-fitting, and manages to sufficiently estimate the permittivity profile and the underlying layered structure in an efficient manner (see Figure 1c). Small errors observed in Figure 1c can be due to: the linear-path simplification; manual picking of the hyperbolas (Ding et al., 2020); non-accurate time-zero correction (Yelf, 2004); and/or non-ideal targets that is, $R \neq 0$. From Figure 1c, it is apparent that conventional hyperbola fitting using the Dix conversion overestimates the resulting permittivity and fails to reconstruct complex velocity profiles despite the dense velocity sampling (nine hyperbolas) used in the numerical case studies.

Typical hyperbola fitting using the Dix conversion (see Text S1) is based on the assumption that the investigated medium consists of homogeneous horizontal layers (Dix, 1955). The number of layers equals the number of apparent velocities used in the conversion. For example, if five hyperbolas are used, then the underlying assumption is that the investigated medium consists of five homogeneous layers. In the presence of numerous layers or smooth variations of velocity, the Dix conversion requires a large number of hyperbolas in order to accurately reconstruct the 1D velocity profile. The proposed methodology overcomes this limitation by assuming a smooth velocity profile. The latter is independent to the number of hyperbolas used. The resulting model using our approach is the optimized 1D velocity profile that satisfies the measured hyperbolas.

2.3. Results From Chang'E-4 Channel 2 Data

The proposed methodology is applied to the high frequency data collected by the Yutu-2 rover at the VK crater during the first two lunar days of the Chang'E-4 mission (Li et al., 2020). During the first two lunar days, the rover followed an irregular path and managed to cover ~ 106 m (Li et al., 2020). The current paper focuses on the first 150 ns of the scan in order to effectively map the shallow layers (~ 10 – 12 m) of the regolith. Based on the results, a revised stratigraphy for the VK crater is proposed (in the next chapter) that takes into account a previously unseen layered structure within the first ~ 10 m of lunar regolith.

The radargram was processed using a typical GPR processing pipeline that involves zero-time correction, dewow, time-gain (exponential gain), and background removal (Cassidy, 2009). The resulting B-Scan for the first 150 ns is illustrated in Figure 2 (Li et al., 2020). The overall signal to clutter ratio is substantially higher compared to Chang'E-3 mission (Lai et al., 2019; Li et al., 2020) (potentially due to lack of ilmenite) which results in clear hyperbolic features that can be utilized to deduce the shallow layered structure at the first 10–12 m of the landing site.

Figure 2a illustrates the resulting relative permittivity profile using the proposed advanced hyperbola-fitting, subject to the hyperbolas shown in Figure 2b. It is evident that there is a layered structure with four layers in the first 10 m of the regolith. The first and the third layers have low permittivity values while the second and the fourth layers have permittivity up to $\epsilon \approx 10$ (see Figure 2a). Typical lunar soils have low permittivity values although there are reported high-density lunar samples with relative permittivity up to $\epsilon \approx 10$ (Chung et al., 1970; Olhoeft & Strangway, 1975). To further evaluate the validity of these results a sensitivity analysis is presented in Figures S3 and S4 where it is shown that the permittivity value for the low permittivity layers can range between $\epsilon \sim 1.7 - 2.3$ without compromising accuracy. For the high permittivity layers, there is an optimisation plateau at $\epsilon \sim 8 - 10$ where there is no significant error improvement.

We would like to highlight that current knowledge regarding the permittivity of lunar soils is based primarily on shallow samples brought back to Earth during the Apollo missions. Superficial lunar samples are not representative of deeper layers since they are exposed to impact gardening. The latter, results in an increased porosity (Horz et al., 1991) and vitrification (Nash & Conel, 1973). Increased porosity decreases the overall permittivity of multi-phase media (Dobson et al., 1985; Hallikainen et al., 1985; Peplinski et al., 1995), which results in a well-known causal relationship between permittivity and density (Chung

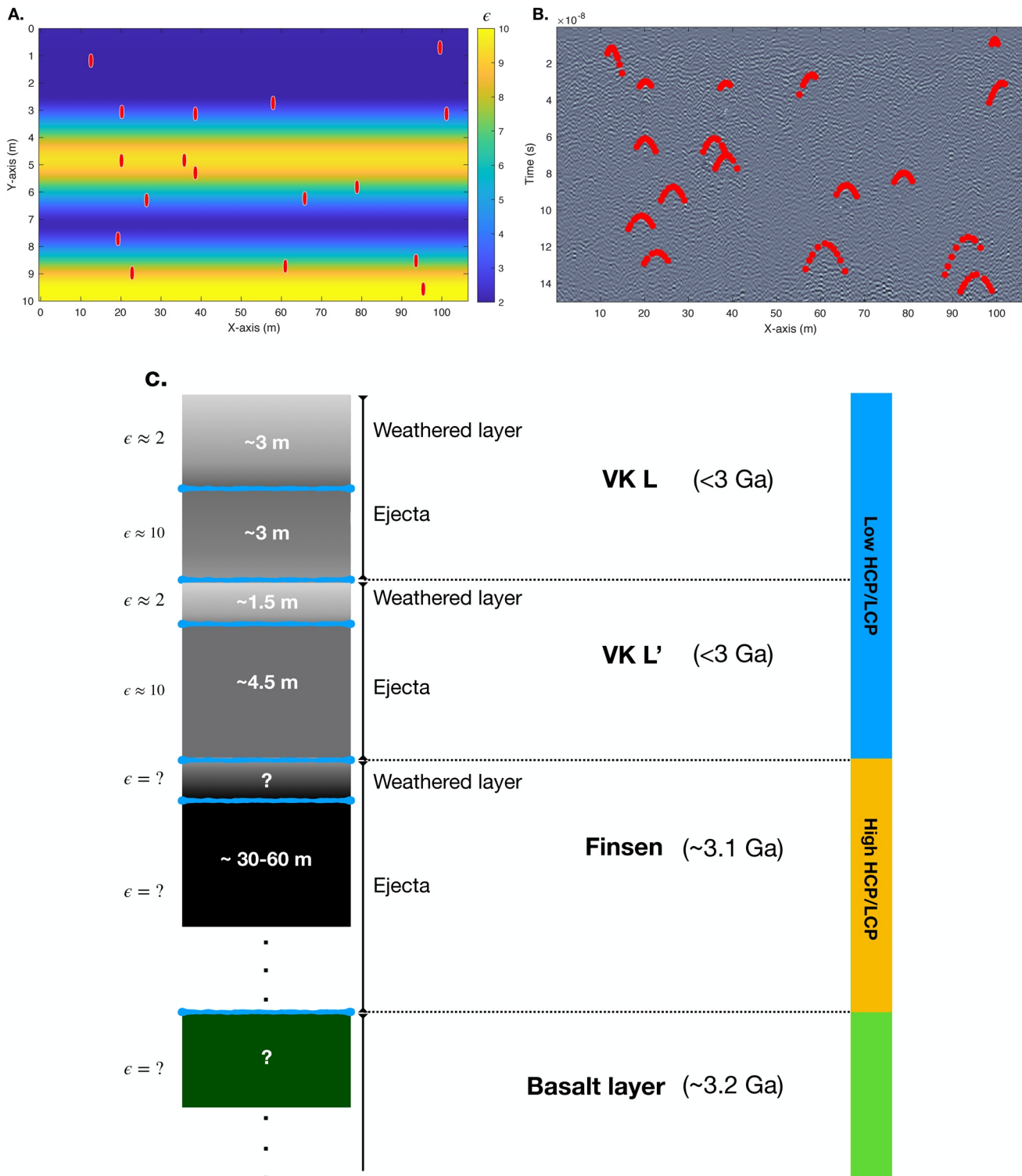


Figure 2. (a) The resulting relative permittivity profile $\epsilon(y)$ at the landing site of Chang'E-4 mission using the advanced hyperbola fitting. The coordinates of the investigated targets are illustrated with red dots. (b) The fitted hyperbolas subject to the permittivity profile shown in panel (a). More details regarding the fitted hyperbolas can be found in Figure S6. (c) The proposed stratigraphy model for the Chang'E-4 landing site. The first ~6 m consists of a top weathered layer overlaying the ejecta from VK L crater. Below that, is a low permittivity layer that corresponds to the weathered ejecta of the VK L' crater. The VK L' ejecta extends to ~12 m depth, where the Finsen and Alder ejecta lay on top of the Imbrian basaltic layer. Dates are based on Lu et al. (2021) and the chemical composition on Huang et al. (2018).

et al., 1970; Olhoeft & Strangway, 1975). In addition, vitrification transforms lunar materials to glassy fragments that have lower permittivity values compared to typical lunar minerals (pyroxenes, plagioclase, olivine, ilmenite etc.) (Campbell & Ulrichs, 1969). The lunar regolith is, therefore, a low permittivity medium, established through laboratory (Carrier et al., 1991), satellite (Bhattacharya et al., 2015; Gong et al., 2015), and in-situ measurements (Dong et al., 2021). The semi-empirical models tuned for lunar soils are primarily based on shallow regolith samples (Carrier et al., 1991; Chung et al., 1970; Frisillo et al., 1975; Shkuratov & Bondarenko, 2001). The latter are affected by impact gardening making them unreliable for estimating the dielectric properties of deeper ejecta. Estimation of the dielectric properties of deeper layers is still an ongoing research area that is, primarily based on LPR measurements and typical hyperbola-fitting (Dong, Feng, Zhao, et al., 2020). An indirect method to infer the permittivity is using the Complex Refractive Index Model (CRIM) which is a mainstream formula for computing the bulk permittivity of multi-phase media (Birchak et al., 1974) based on the permittivity of their components. Typical minerals in lunar soils are pyroxene, plagioclase, olivine and ilmenite (Zongcheng et al., 2015). The relative electric permittivity of plagioclase is $\epsilon_{pl} \approx 6.5$ (Zheng et al., 2005). The relative permittivity of pyroxene varies from $\epsilon_{py} \approx 7 - 10$ (Campbell & Ulrichs, 1969; Zheng et al., 2005), in particular for augite and for pyroxenes in anorthosites the relative permittivity can be as high as $\epsilon_{py} \approx 11$ (Zheng et al., 2005). The relative permittivity of olivine is $\epsilon_{ol} \approx 8$ (Zheng et al., 2005) and for ilmenite $\epsilon_{il} \approx 50$ (Zheng et al., 2005). Using CRIM, it can be proven, that some realistic mineralogical composition can give rise to high permittivity values for example, $V_{air} = 10\%$, $V_{il} = 8\%$, $V_{pl} = 40\%$, $V_{py} = 42\%$. The aforementioned soil sample has bulk relative permittivity (estimated using CRIM) $\epsilon \approx 9$. High relative permittivity values as high as $\epsilon = 8.9$ have also been calculated via hyperbola fitting at Chang'E-3 landing site (Lai et al., 2016).

3. Stratigraphy of the Landing Site

3.1. Geological Background

The Chinese lunar probe Chang'E-4, carrying the Yutu-2 rover, was the first human-made object that landed on the far-side of the Moon on 3rd of January 2019 (Li et al., 2019; Tang et al., 2020). The landing site is located at the South Pole-Aitkens (SPA) basin—the oldest and biggest crater on the Moon (Huang et al., 2018; Hu et al., 2019; James et al., 2019). The SPA basin is pre-Nectarian in age and has an elliptical shape (Garrick-Bethell & Zuber, 2009) with an approximate diameter of 2,100–2,500 km (Moriarty et al., 2013). The transient cavity of the SPA basin has been estimated between 840 and 1,400 km (Moriarty et al., 2013; Potter et al., 2012). The maximum excavation depth of lunar craters with a diameter below <10 km is approximately 10% of their diameter (Stopar et al., 2017). There is an ongoing debate whether or not this ratio holds true for larger craters (Potter et al., 2012; Wieczorek & Phillips, 1999). Simulations suggest that this ratio can be extrapolated for craters with diameter up to 1,100 km (Potter et al., 2012) while gravity measurements indicate that this ratio decreases for craters with diameter >500 km (Wieczorek & Phillips, 1999). The above, suggest that the SPA basin might have excavated through lunar crust and into the mantle (Hammond et al., 2009; Hurwitz & Kring, 2014; Melosh et al., 2017; Moriarty et al., 2013, 2021; Uemoto et al., 2017; Vaughan & Head, 2014). This premise is based on the maximum depth of lunar crust ~60 km (~45 km on the far-side [Moriarty et al., 2021]), as estimated by the Gravity Recovery and Interior Laboratory mission (Wieczorek et al., 2013), which is in good agreement with seismic data from the Apollo missions (Khan, 2002). The shallow mantle layer was most likely melted during the impact (Hurwitz & Kring, 2014; Melosh et al., 2017; Moriarty et al., 2013, 2021; Potter et al., 2012; Vaughan & Head, 2014) and parts of it are expected to occur within the SPA basin, forming an underlying sheet of non-crustal materials (Moriarty et al., 2013, 2021; Potter et al., 2012). These materials are of paramount importance since they can constrain the composition of the upper mantle and provide an insight into the early evolution of the Moon (Moriarty et al., 2013; Yamamoto et al., 2010).

Based on previous models of lunar evolution—that suggest an upper mantle predominantly composed of olivine (Charlier et al., 2018; Y. Lin et al., 2017; Moriarty et al., 2021; Snyder et al., 1992; Yamamoto et al., 2010)—strong spectral signatures of olivine were expected to be present within SPA (Ivanov et al., 2018; Lucey, 2004; Moriarty et al., 2021). Nonetheless, data from CLEMENTINE and SELENE did not support this premise (Lemelin et al., 2019; Matsunaga et al., 2008; Tompkins & Pieters, 1999; Yamamoto et al., 2010), apart from small occurrences of olivine clusters (Lemelin et al., 2019; Yamamoto et al., 2010)

most likely originated from crustal materials, due to their location (the exterior of the SPA) and the high content of feldspar in their near proximity (Moriarty & Pieters, 2018). Remote sensing data from the peak of craters indicate that SPA is dominated by mg-rich orthopyroxene (Moriarty & Pieters, 2018; Nakamura et al., 2009). Many different theories have been proposed to explain the unexpected lack of olivine and the abundance of pyroxene (Ivanov et al., 2018). Low olivine content supports the premise that SPA did not penetrate through the crust (Lucey, 2004) due to an oblique impact (Garrick-Bethell & Zuber, 2009; Schultz & Crawford, 2011). Lack of olivine can also be explained by a pyroxene-rich composition of the upper mantle (Kuskov O.L., 2015; Melosh et al., 2017). Moreover, the large impact that created SPA could potentially cause large lava bodies that undergo fractional crystallization which can lead to the separation and sinking of olivine and the accumulation of pyroxene at the top (Hurwitz & Kring, 2014; Vaughan & Head, 2014). The SPA is dominated by mafic materials and in particular by Mg-rich and low-Ca pyroxene (Huang et al., 2018; Moriarty & Pieters, 2015, 2018; Nakamura et al., 2009). CLEMENTINE measurements reveal an inner zone with Fe abundance and an outer zone with lower Fe content (Jolliff et al., 2000; Lucey et al., 1998; Moriarty & Pieters, 2018). Furthermore, using data from the Moon Mineralogy Mapper (M^3), Moriarty and Pieters (2018) have divided the SPA into four zones. The first zone is the inner SPA area called SPACA, with characteristic Ca-pyroxene abundance that lies at the center of the SPA. The second zone surrounds SPACA, and it is an area with Mg-rich pyroxenes. Based on spectral analysis of the central peaks of the craters within SPACA, strong indications were given to support the premise that SPACA lies on top of the Mg-rich area (Moriarty & Pieters, 2015, 2018). The third zone is a heterogeneous annulus that consists of pyroxene and feldspar, and acts as the intermediate stage between the SPA and its exterior. The latter is the fourth zone, a mafic-free area with high content of feldspar, similar to lunar highlands (Moriarty & Pieters, 2015, 2018).

The landing site of Chang'E-4 is within the Mg-rich annulus (Moriarty & Pieters, 2018) and in particular in the interior of the VK crater (177.588°E, 45.4578°S, see Figure S5) (Di et al., 2019; Li, 2021; Li et al., 2020; Qiao et al., 2019; Zhang et al., 2020). VK is an elliptical crater (Zhang et al., 2020) with approximately ~186 km diameter (Guo et al., 2021; Huang et al., 2018). The age of VK was estimated pre-Nectarian (Huang et al., 2018; Losiak et al., 2009) and recent studies have placed it at ~4.2 Ga (Lu et al., 2021), very close to the formation of SPA (Garrick-Bethell & Miljković, 2018; Hiesinger et al., 2012; Lu et al., 2021). The creation of Leibnitz crater affected the north part of VK and contributed to the ejecta layer prior to the Imbrian basaltic flood (Huang et al., 2018; Yingst et al., 2017). Ejecta from Alder crater (widely accepted as an Imbrian crater (Losiak et al., 2009) and recently dated at ~3.5 Ga [Lu et al., 2021]) are also expected to the pre-basaltic layers (Huang et al., 2018; Lu et al., 2021). The VK crater was flooded with basalts during the Imbrian period (Huang et al., 2018; Paskert et al., 2018) around ~3.2–3.3 Ga (Haruyama et al., 2009; Lu et al., 2021). The ejecta from Finsen crater are expected to have contributed to the post-Imbrian VK layers (Huang et al., 2018). Finsen is an Eratosthenian crater (Losiak et al., 2009; Wilhelm & McCauley, 1987) and its ejecta and floor are dated at ~3.1 and 3 Ga respectively (Lu et al., 2021). Recent studies suggest that Orientale crater might have added to the post-Imbrian VK layers as well (Xiao et al., 2021). Subsequently, the Eratosthenian craters VK L and L' were formed (Paskert et al., 2018; Zhang et al., 2020). The VK, Leibnitz, Alder, VK L, and L' lie within the Mg-pyroxene annulus while Finsen is within the SPACA region (Moriarty & Pieters, 2018).

Geological context suggests that the craters VK L, L', Finsen and Orientale have contributed to most of the post-Imbrian ejecta layers of the VK crater (Huang et al., 2018; Di et al., 2019; Paskert et al., 2018; Xiao et al., 2021). The thickness of the Finsen ejecta at the area of the Chang'E-4 landing site is estimated—via numerical simulations (Di et al., 2019)—at ~30 m. This is not in good agreement with the results obtained using dark-halo and non-dark halo craters (Guo et al., 2021; Li et al., 2020) that suggest a thicker post-basaltic layer, probably due to the presence of Orientale ejecta (Xiao et al., 2021). Nonetheless, contradicting data (Yue et al., 2020) place the date of Orientale to be older than the Imbrian basaltic flood, which implies that there might be another source that contributed to the post-basaltic VK layers, probably additional ejecta from the Eratosthenian craters (VK L and L') at the rim of VK (Paskert et al., 2018).

The surface of the landing site is smooth with a small number of boulders (Ding et al., 2020; Weiren et al., 2019), most of them being glassy fragments and breccias from secondary craters (H. Lin et al., 2020). From in situ reflectance data, the visible surface at the landing site is not olivine-pyroxene rich and consists

of 56%–72% plagioclase, similar to lunar highlands (Hu et al., 2019; Li et al., 2019) with Mg-rich orthopyroxene (Gou et al., 2020; Huang et al., 2018). The thickness of the regolith (weathered top soil) is estimated using LROC NAC images at ~2.5–7.5 m (Huang et al., 2018) using the technique described by (Quaide William & Oberbeck, 1968). Based on the M^3 reflectance data, it is estimated that below the top weathered soil, lays a low-calcium pyroxene (LCP) layer (Gou et al., 2019; Li et al., 2019) ranging from ~8–13 m followed by a high-calcium pyroxene (HCP) layer from ~13–53 m (Huang et al., 2018).

3.2. Previous Studies Using LPR Data

Further insights on the ejecta at the VK crater are provided by the LPR mounted to the Yutu-2 rover of the Chang'E-4 mission (Li et al., 2020). The first attempt to examine the lunar surface with in-situ LPR equipment occurred during the Chang'E-3 mission on the near side of the moon (Ding et al., 2020; Fa et al., 2015; Lai et al., 2019; Yuan et al., 2017). Similar antenna configurations were employed for both Chang'E-3 and Chang'E-4 missions (Li et al., 2020). In particular, two antennas with 500 MHz central frequency (at the bottom of the rover), and one low frequency antenna (mounted at the back of the rover) with 60 MHz central frequency (Li et al., 2020). The low frequency antenna from the Chang'E-4 mission gave thin indications of four different lava flows that probably occurred during the Imbrian period (Lai et al., 2020). Unfortunately, the low frequency data in both missions suffer from ringing noise due to the coupling between the antenna and the rover, which resulted in erroneous reflections and noisy data (Li et al., 2018; Zhang et al., 2020). In contrast to the Chang'E-3 landing site (Lai et al., 2019), in the VK crater, the ilmenite content is fairly low, making the ejecta layers transparent to LPR (Dong, Feng, Zhao, et al., 2020). This resulted in good quality data that clearly demonstrated a complex layered structure for the first 50 m of the VK crater (Li et al., 2020; Zhang et al., 2020). In addition, using a conventional hyperbola-fitting (assuming a homogeneous medium) with Dix conversion, the electric permittivity of the ejecta layers was estimated, and furthermore used to infer the mineralogical (Fe and Ti content) (Li et al., 2020) and the mechanical (density) properties of the lunar regolith (Dong, Feng, Zhao, et al., 2020; Dong, Feng, Zhou, et al., 2020), based on semi-empirical formulas fine-tuned for lunar soils (Carrier et al., 1991; Hickson et al., 2018; Olhoeft & Strangway, 1975). The relative electric permittivity at the landing site monotonically increases from ~3 – 6 with respect to depth, as estimated using typical hyperbola fitting (Dong, Feng, Zhao, et al., 2020). This corresponds to a density that starts from ~1 gr / cm^3 at the surface and reaches 2.5 gr / cm^3 at 50 m depth (Dong, Feng, Zhao, et al., 2020).

3.3. Revised Stratigraphic Column Using Advanced Hyperbola Fitting

The suggested stratigraphy model is based on the LPR results shown in Figure 2a and the following premises:

1. Finsen, VK L and L' craters are the predominant sources of the post-Imbrian ejecta in the VK crater (Huang et al., 2018; Paskert et al., 2018; Zhang et al., 2020).
2. Finsen crater was developed before VK L and L' craters (Huang et al., 2018; Zhang et al., 2020).
3. Finsen ejecta at the landing site are estimated via numerical simulations at ~30 m (Di et al., 2019).
4. The thickness of the weathered top soil was calculated at ~2.5 – 7.5 m (Huang et al., 2018) using the geometrical method described in (Quaide William & Oberbeck, 1968). This is consistent with the average regolith growth rate (~1.5 m/Ga) from ~3.5 Ga to the present day (Gou et al., 2021; Horz et al., 1991; Oberbeck & Quaide, 1968; Quaide & Oberbeck, 1975).
5. Below the weathered top soil there is an LCP layer down to ~13 m (Gou et al., 2019; Huang et al., 2018; Li et al., 2019).
6. Below the LCP layer there is a thick layer (>30 m) with high HCP/LCP ratio (Huang et al., 2018).
7. Finsen crater is within the SPACA region and therefore it is expected that its excavated materials have an increased HCP/LCP ratio (Moriarty & Pieters, 2018).
8. The ejecta materials from VK L and L' craters have low HCP/LCP ratio (Huang et al., 2018; Hu et al., 2019; Ling et al., 2019).
9. There is a clear sharp boundary observed on LPR data (Dong, Feng, Zhou, et al., 2020; Li et al., 2020; Zhang et al., 2020) at ~13 m, most-likely between the LCP and the HCP layer.

The proposed stratigraphy model suggests that the HCP layer overlying the Imbrian basalts is the ejecta from the Finsen crater (Huang et al., 2018); and maybe Orientale crater too (Xiao et al., 2021). This premise is consistent both with the size of this layer (as predicted by numerical simulations [Di et al., 2019]) and with the chemical composition of the Finsen crater (Moriarty & Pieters, 2018; Moriarty et al., 2011). On top of the Finsen ejecta, it is expected to encounter ejecta from Eratosthenian post-Finsen craters. A homogeneous weathered layer with 12 m depth as suggested by Zhang et al. (2020) is not consistent with LROC NAC images that points to a ~ 2.5 – 7.5 m regolith (Huang et al., 2018) and by the layered structure revealed by the proposed hyperbola-fitting scheme (see Figure 2a). In addition, a 12–13 m regolith indicates a regolith growth rate of ~ 3 – 4 m/Ga which is twice as fast compared to the growth rate expected from ~ 3.5 Ga to the present day (Gou et al., 2021; Horz et al., 1991; Oberbeck & Quaide, 1968; Quaide & Oberbeck, 1975). In general, the average regolith depth in mare areas is expected to be around ~ 4 – 5 m while a ~ 10 – 15 m regolith is more common in old lunar highlands (McKay et al., 1991).

We propose that the top ~ 10 – 12 m of the landing site consists of ejecta from the VK L and L' craters. This is in good agreement with the LCP content of the VK L and L' craters (Huang et al., 2018; Hu et al., 2019; Ling et al., 2019) and with the layered structure illustrated in Figure 2a. The suggested stratigraphic model of the post-basaltic flood ejecta of VK crater is shown in Figure 2c. The ejecta of VK L' (≈ 5.5 m) were deposited on top of the Finsen ejecta at early Eratosthenian. Impact gardening degraded the first ~ 1.5 m of the ejecta decreasing its density (Horz et al., 1991) and consequently its electric permittivity (due to the causal relationship between permittivity and density [Chung et al., 1970; Olhoeft & Strangway, 1975]). The width of the VK L' regolith is in good agreement with the literature which suggests that rapid gardening is expected at young ejecta, a phenomenon that has also been observed at the Chang'E-3 landing site (Fa et al., 2015; Gou et al., 2021). The ejecta from VK L is subsequently deposited on top of the weathered layer creating a top layer with ~ 6 m width. The long gardening process, from early Eratosthenian till now, gave rise to a ~ 3 m of loose lunar soil with low electric permittivity as predicted by Figure 2a. This is in good agreement with the regolith thickness as estimated using LROC NAC images (Huang et al., 2018); and also with the average regolith growth rate (~ 1.5 m/Ga) expected from ~ 3.5 Ga to the present day (Gou et al., 2021; Horz et al., 1991; Oberbeck & Quaide, 1968; Quaide & Oberbeck, 1975).

4. Conclusions

A novel interpretation tool was described capable of estimating the permittivity profile of the shallow lunar surface using LPR. The validity and the superiority of the suggested scheme compared to typical hyperbola-fitting was demonstrated via a set of numerical experiments that have clearly shown that the proposed scheme is capable of reconstructing complicated permittivity profiles using the shape of multiple hyperbolas as the only inputs. The proposed methodology is suitable for any arbitrary one-dimensional permittivity distribution, which makes it an appealing choice for inferring the dielectric properties of the lunar regolith. The advanced hyperbola-fitting was applied to the high frequency data collected during the first two lunar days of the Chang'E-4 mission. The resulting permittivity profile indicates a layered structure within the first 10 m of the regolith. These shallow layers are not visible in the measured radargram due to the smooth boundaries between them, making them undetectable using traditional signal processing approaches. It is argued that the multiple layers detected within the shallow lunar regolith can be the ejecta of the Eratosthenian craters VK L and L', laying on top of the late-Imbrian ejecta of Finsen crater.

Data Availability Statement

The images shown in Figure S5 are available from the Lunar Reconnaissance Orbiter's Wide Angle Camera. Image Credit: NASA, GSFC, Arizona State Univ. Lunar Reconnaissance Orbiter, available at: <https://apod.nasa.gov/apod/ap161230.html>. The Chang'E-4 Lunar Penetrating Radar data are available from the Data Publishing and Information Service System of China Lunar Exploration Program at: http://moon.bao.ac.cn/index_en.jsp, https://moon.bao.ac.cn/searchOrder_dataSearchData.search. The specific files used here are listed in Table S1 and are as follows: CE4_GRAS_LPR-2B_SCI_N_20190104004000_20190109213900_0001_A.2B; CE4_GRAS_LPR-2B_SCI_N_20190109213901_20190111150200_0002_A.2B; CE4_GRAS_LPR-2B_SCI_N_20190111150201_20190112102100_0003_A.2B; CE4_GRAS_LPR-2B_SCI_N_20190131080301_

20190201054300_0005_A.2B; CE4_GRAS_LPR-2B_SCI_N_20190201054301_20190208101200_0006_A.2B; CE4_GRAS_LPR-2B_SCI_N_20190208101201_20190209053100_0007_A.2B; CE4_GRAS_LPR-2B_SCI_N_20190209053101_20190209130800_0008_A.2B; CE4_GRAS_LPR-2B_SCI_N_20190209130801_20190210033400_0009_A.2B; CE4_GRAS_LPR-2B_SCI_N_20190210033401_20190211100800_0010_A.2B.

Acknowledgments

None.

References

- Aldo, V. (1996). Ray tracing based on Fermat's principle in irregular grids. *Geophysical Prospecting*, 44(5), 741–760.
- Bano, M. (2006). Effects of the transition zone above a water table on the reflection of GPR waves. *Geophysical Research Letters*, 33(13), L13309. <https://doi.org/10.1029/2006gl026158>
- Bhattacharya, A., Porwal, A., Dhingra, S., De, S., & Venkataraman, G. (2015). Remote estimation of dielectric permittivity of lunar surface regolith using compact polarimetric synthetic aperture radar data. *Advances in Space Research*, 56(11), 2439–2448. <https://doi.org/10.1016/j.asr.2015.10.007>
- Birchak, J. R., Gardner, C. G., Hipp, J. E., & Victor, J. M. (1974). High dielectric constant microwave probes for sensing soil moisture. *Proceedings of the IEEE*, 62(1), 93–98. <https://doi.org/10.1109/PROC.1974.9388>
- Boero, F., Fedeli, A., Lanini, M., Maffongelli, M., Monleone, R., Pastorino, M., et al. (2018). Microwave tomography for the inspection of wood materials: Imaging system and experimental results. *IEEE Transactions on Microwave Theory and Techniques*, 66(7), 3497–3510. <https://doi.org/10.1109/tmtt.2018.2804905>
- Campbell, M. J., & Ulrichs, J. (1969). Electrical properties of rocks and their significance for lunar radar observations. *Journal of Geophysical Research*, 74(25), 5867–5881. <https://doi.org/10.1029/jb074i025p05867>
- Carrier, W. D., Olhoeft, G. R., & Mendell, W. (1991). Physical properties of the lunar surface. In *Lunar sourcebook* (pp. 522–530).
- Cassidy, N. J. (2009). Chapter 5 - Ground penetrating radar data processing, modelling and analysis. In H. M. Jol (Ed.), *Ground penetrating radar theory and applications* (pp. 141–176). Amsterdam: Elsevier. <https://doi.org/10.1016/b978-0-444-53348-7.00005-3>
- Charlier, B., Grove, T. L., Namur, O., & Holtz, F. (2018). Crystallization of the lunar magma ocean and the primordial mantle-crust differentiation of the moon. *Geochimica et Cosmochimica Acta*, 234, 50–69. <https://doi.org/10.1016/j.gca.2018.05.006>
- Chung, D. H., Westphal, W. B., & Simmons, G. (1970). Dielectric properties of Apollo 11 lunar samples and their comparison with Earth materials. *Journal of Geophysical Research*, 75(32), 6524–6531. <https://doi.org/10.1029/jb075i032p06524>
- Conyers, L. B. (2004). *Ground penetrating radar for archaeology*. Walnut Creek, CA, USA: AltaMira Press.
- Daniels, D. J. (2004). *Ground penetrating radar*. U.K: Institution of Engineering and Technology.
- Di, K., Zhu, M. H., Yue, Z., Lin, Y., Wan, W., Liu, Z., & Xue, B. (2019). Topographic evolution of Von Kármán crater revealed by the lunar rover Yutu-2. *Geophysical Research Letters*, 46, 12764–12770. <https://doi.org/10.1029/2019gl085252>
- Diamanti, N., Annan, A. P., & Redman, J. D. (2014). Impact of gradational electrical properties on GPR detection of interfaces. In *Proceedings of the 15th international conference on ground penetrating radar* (pp. 529–534). <https://doi.org/10.1109/icgpr.2014.6970480>
- Ding, C., Xiao, Z., Su, Y., & Cui, J. (2020). Hyperbolic reflectors determined from peak echoes of ground penetrating radar. *Icarus*, 358, 114280.
- Dix, C. H. (1955). Seismic velocities from surface measurements. *Geophysics*, 20, 68–86. <https://doi.org/10.1190/1.1438126>
- Dobson, M. C., Ulaby, F. T., Hallikainen, M. T., & El-rayes, M. A. (1985). Microwave dielectric behavior of wet soil-part ii: Dielectric mixing models. *IEEE Transactions on Geoscience and Remote Sensing*, 23(1), 35–46. <https://doi.org/10.1109/tgrs.1985.289498>
- Dong, Z., Fang, G., Zhou, B., Zhao, D., Gao, Y., & Ji, Y. (2021). Properties of lunar regolith on the moon's farside unveiled by chang'e-4 lunar penetrating radar. *Journal of Geophysical Research: Planets*, 126(6), e2020JE006564. <https://doi.org/10.1029/2020je006564>
- Dong, Z., Feng, G., Zhao, D., Zhou, B., Gao, Y., & Ji, Y. (2020). Dielectric properties of lunar subsurface materials. *Geophysical Research Letters*, 47, e2020GL089264. <https://doi.org/10.1029/2020gl089264>
- Dong, Z., Feng, X., Zhou, H., Liu, C., Zeng, Z., Li, J., & Liang, W. (2020). Properties analysis of lunar regolith at Chang'E-4 landing site based on 3d velocity spectrum of lunar penetrating radar. *Remote Sensing*, 12, 629. <https://doi.org/10.3390/rs12040629>
- Fa, W. (2020). Bulk density of the lunar regolith at the Chang'E-3 landing site as estimated from lunar penetrating radar. *Earth and Space Science*, 7(2), e2019EA000801. <https://doi.org/10.1029/2019ea000801>
- Fa, W., Zhu, M.-H., Liu, T., & Plescia, J. B. (2015). Regolith stratigraphy at the chang'e-3 landing site as seen by lunar penetrating radar. *Geophysical Research Letters*, 42(23), 10179–10187. <https://doi.org/10.1002/2015gl066537>
- Feng, X., Sato, M., & Liu, C. (2012). Subsurface imaging using a handheld GPR md system. *IEEE Geoscience and Remote Sensing Letters*, 9(4), 659–662. <https://doi.org/10.1109/lgrs.2011.2177514>
- Frisillo, A. L., Olhoeft, G. R., & Strangway, D. W. (1975). Effects of vertical stress, temperature and density on the dielectric properties of lunar samples 72441, 12, 15301, 38 and a terrestrial basalt. *Earth and Planetary Science Letters*, 24, 345–356. [https://doi.org/10.1016/0012-821x\(75\)90140-5](https://doi.org/10.1016/0012-821x(75)90140-5)
- Garrick-Bethell, I., & Miljković, K. (2018). Age of the lunar South Pole Aitken basin. In *Lunar and planetary science conference*.
- Garrick-Bethell, I., & Zuber, M. T. (2009). Elliptical structure of the lunar South Pole-Aitken basin. *Icarus*, 204(2), 399–408. <https://doi.org/10.1016/j.icarus.2009.05.032>
- Giannakis, I., Giannopoulos, A., & Warren, C. (2016). A realistic FDTD numerical modeling framework of ground penetrating radar for landmine detection. *IEEE Journal of Selected Topics in Applied Earth Observations and Remote Sensing*, 9(1), 37–51. <https://doi.org/10.1109/jstars.2015.2468597>
- Giannakis, I., Giannopoulos, A., & Warren, C. (2019). A machine learning-based fast-forward solver for ground penetrating radar with application to full-waveform inversion. *IEEE Transactions on Geoscience and Remote Sensing*, 57(7), 4417–4426. <https://doi.org/10.1109/tgrs.2019.2891206>
- Giannakis, I., Giannopoulos, A., & Warren, C. (2020). A machine learning scheme for estimating the diameter of reinforcing bars using ground penetrating radar. *IEEE Geoscience and Remote Sensing Letters*, 18, 461–465.
- Giannopoulos, A. (2008). An improved new implementation of complex frequency shifted PML for the FDTD method. *IEEE Transactions on Antennas and Propagation*, 56(9), 2995–3000. <https://doi.org/10.1109/tap.2008.928789>
- Gong, X., Paige, D. A., Siegler, M. A., & Jin, Y.-Q. (2015). Inversion of dielectric properties of the lunar regolith media with temperature profiles using chang'e microwave radiometer observations. *IEEE Geoscience and Remote Sensing Letters*, 12(2), 384–388. <https://doi.org/10.1109/LGRS.2014.2343617>

- Gou, S., Di, K., Yue, Z., Liu, Z., He, Z., Xu, R., et al. (2019). Lunar deep materials observed by chang'e-4 rover. *Earth and Planetary Science Letters*, 528, 115829. <https://doi.org/10.1016/j.epsl.2019.115829>
- Gou, S., Di, K., Yue, Z., Liu, Z., He, Z., Xu, R., et al. (2020). Forsteritic olivine and magnesium-rich orthopyroxene materials measured by Chang'E-4 rover. *Icarus*, 345, 113776. <https://doi.org/10.1016/j.icarus.2020.113776>
- Gou, S., Yue, Z., Di, K., Cai, Z., Liu, Z., & Niu, S. (2021). Absolute model age of lunar finsen crater and geologic implications. *Icarus*, 354, 114046. <https://doi.org/10.1016/j.icarus.2020.114046>
- Guo, D., Fa, W., Zeng, X., Du, J., & Liu, J. (2021). Geochemistry of the von kármán crater floor and thickness of the non-mare ejecta over the chang'e-4 landing area. *Icarus*, 359, 114327. <https://doi.org/10.1016/j.icarus.2021.114327>
- Hallikainen, M. T., Ulaby, F. T., Dobson, M. C., El-rayes, M. A., & Wu, L. (1985). Microwave dielectric behavior of wet soil-part 1: Empirical models and experimental observations. *IEEE Transactions on Geoscience and Remote Sensing*, 23(1), 25–34. <https://doi.org/10.1109/tgrs.1985.289497>
- Hammond, N., Nimmo, F., & Korycansky, D. (2009). Hydrocode modeling of the South Pole Aitken basin-forming impact. In *Lunar and planetary sciences conference (LPSC)*.
- Hansen, P. C. (1992). Analysis of discrete ill-posed problems by means of the l-curve. *SIAM Review*, 34, 561–580. <https://doi.org/10.1137/1034115>
- Haruyama, J., Ohtake, M., Matsunaga, T., Morota, T., Honda, C., Yokota, Y., et al. (2009). Long-lived volcanism on the lunar farside revealed by selenite terrain camera. *Science*, 323(5916), 905–908. <https://doi.org/10.1126/science.1163382>
- Hickson, D., Boivin, A., Daly, M. G., Ghent, R., Nolan, M. C., Tait, K., & Tsai, C. A. (2018). Near surface bulk density estimates of NEAs from radar observations and permittivity measurements of powdered geologic material. *Icarus*, 306. <https://doi.org/10.1016/j.icarus.2018.01.018>
- Hiesinger, H., vander Bogert, C. H., Pascker, J. H., Schmedemann, N., Robinson, M. S., Jolliff, B., & Petro, N. (2012). New crater size-frequency distribution measurements of the South Pole Aitken basin. In *Lunar and planetary science conference*.
- Horz, F., Grive, R. A. F., Heiken, G., Spudis, P. D., & Binder, A. B. (1991). Lunar surface processes. In G. Heiken, D. Vaniman, & B. M. French (Eds.), *Lunar sourcebook* (Vol. 121, pp. 61–120). New York: Cambridge University Press.
- Hu, X., Ma, P., Yang, Y., Zhu, M., Jiang, T., Lucey, P. G., et al. (2019). Mineral abundances inferred from in situ reflectance measurements of Chang'E-4 landing site in South-Pole Atkins. *Geophysical Research Letters*, 46, 9439–9447. <https://doi.org/10.1029/2019gl084531>
- Huang, J., Xiao, Z., Flahaut, J., Martinot, M., Head, J., Xiao, X., et al. (2018). Geological characteristics of Von Kármán crater, north-western South Pole-Aitken basin: Chang'E-4 landing site region. *Journal of Geophysical Research: Planets*, 123, 1684–1700. <https://doi.org/10.1029/2018je005577>
- Hurwitz, D. M., & Kring, D. A. (2014). Differentiation of the South Pole–Aitken basin impact melt sheet: Implications for lunar exploration. *Journal of Geophysical Research: Planets*, 119(6), 1110–1133. <https://doi.org/10.1002/2013JE004530>
- Ivanov, M. A., Hiesinger, H., van derBogert, C. H., Orgel, C., Pasckert, J. H., & Head, J. W. (2018). Geologic history of the northern portion of the South Pole-Aitken basin on the Moon. *Journal of Geophysical Research: Planets*, 123, 2585–2612. <https://doi.org/10.1029/2018je005590>
- James, P. B., Smith, D. E., Byrne, P. K., Kendall, J. D., Melosh, H. J., & Zuber, M. T. (2019). Deep structure of the lunar South Pole-Aitken basin. *Geophysical Research Letters*, 46, 5100–5106. <https://doi.org/10.1029/2019gl082252>
- Jolliff, B. L., Gillis, J. J., Haskin, L. A., Korotev, R. L., & Wieczorek, M. A. (2000). Major lunar crustal terranes: Surface expressions and crust-mantle origin. *Journal of Geophysical Research*, 105, 4197–4216. <https://doi.org/10.1029/1999je001103>
- Kennedy, J., & Eberhart, R. (1995). Particle swarm optimization. In *Proceedings of ICNN'95 - International Conference on Neural Networks*, 4, 1942–1948.
- Khan, A. (2002). An inquiry into the lunar interior: A nonlinear inversion of the Apollo lunar seismic data. *Journal of Geophysical Research*, 107, 3-1–3-23. <https://doi.org/10.1029/2001je001658>
- Kuskov, O. L., Kronrod, E. V., & Kronrod, V. A. (2015). Thermochemical constraints on the thermal state, composition, and mineralogy of the upper mantle of the moon: Evidence from the seismic models. *Solar System Research*, 49, 75–91. <https://doi.org/10.1134/s0038094615010049>
- Lai, J., Xu, Y., Bugiolacchi, R., Meng, X., Xiao, L., Xie, M., et al. (2020). First look by the Yutu-2 rover at the deep subsurface structure at the lunar farside. *Nature Communications*, 11, 3426. <https://doi.org/10.1038/s41467-020-17262-w>
- Lai, J., Xu, Y., Zhang, X., & Tang, Z. (2016). Structural analysis of lunar subsurface with change-3 lunar penetrating radar. *Planetary and Space Science*, 120, 96–102. <https://doi.org/10.1016/j.pss.2015.10.014>
- Lai, J., Xu, Y., Zhang, X., Xiao, L., Yan, Q., Meng, X., et al. (2019). Comparison of dielectric properties and structure of lunar regolith at Chang'e-3 and Chang'e-4 landing sites revealed by ground-penetrating radar. *Geophysical Research Letters*, 46, 12783–12793. <https://doi.org/10.1029/2019gl084458>
- Lauro, S. E., Pettinelli, E., Caprarello, G., Guallini, L., Rossi, A. P., Mattei, E., & R. O. (2020). Multiple subglacial water bodies below the south pole of Mars unveiled by new MARSIS data. *Nature Astronomy*, 5. <https://doi.org/10.1038/s41550-020-1200-6>
- Lemelin, M., Lucey, P. G., Miljković, K., Gaddis, L. R., Hare, T., & Ohtake, M. (2019). The compositions of the lunar crust and upper mantle: Spectral analysis of the inner rings of lunar impact basins. *Planetary and Space Science*, 165, 230–243. <https://doi.org/10.1016/j.pss.2018.10.003>
- Li, C., Liu, D., Liu, B., Ren, X., Liu, J., He, Z., et al. (2019). Chang'e-4 initial spectroscopic identification of lunar far-side mantle-derived materials. *Nature*, 569, 378–382. <https://doi.org/10.1038/s41586-019-1189-0>
- Li, C., Su, Y., Pettinelli, E., Xing, S., Ding, C., Liu, J., & Zhang, H. (2020). The moon's farside shallow subsurface structure unveiled by Chang'E-4 lunar penetrating radar. *Science Advances*, 6(9). <https://doi.org/10.1126/sciadv.aay6898>
- Li, C., Xing, S., Lauro, S. E., Su, Y., Dai, S., Feng, J., et al. (2018). Pitfalls in GPR data interpretation: False reflectors detected in lunar radar cross sections by Chang'E-3. *IEEE Transactions on Geoscience and Remote Sensing*, 56(3), 1325–1335. <https://doi.org/10.1109/tgrs.2017.2761881>
- Li, C., Zuo, W., Wen, W., Zeng, X., Gao, X., Liu, Y., et al. (2021). Overview of the chang'e-4 mission: Opening the frontier of scientific exploration of the lunar far side. *Space Science Reviews*, 217, 35. <https://doi.org/10.1007/s11214-021-00793-z>
- Li, J., Liu, C., Zeng, Z., & Chen, L. (2015). GPR signal denoising and target extraction with the CEEMD method. *IEEE Geoscience and Remote Sensing Letters*, 12(8), 1615–1619. <https://doi.org/10.1109/lgrs.2015.2415736>
- Lin, H., Lin, Y., Yang, W., He, Z., Hu, S., Wei, Y., & Zou, Y. (2020). New insight into lunar regolith forming processes by the lunar rover Yutu-2. *Geophysical Research Letters*, 47, e2020GL087949. <https://doi.org/10.1029/2020gl087949>
- Lin, Y., Tronche, E. J., Steenstra, E. S., & van Westrenen, W. (2017). Evidence for an early wet moon from experimental crystallization of the lunar magma ocean. *Nature Geosciences*, 10, 14–18. <https://doi.org/10.1038/ngeo2845>

- Ling, Z., Qiao, L., Liu, C., Cao, H., Bi, X., Lu, X., et al. (2019). Composition, mineralogy and chronology of mare basalts and non-mare materials in Von Kármán crater: Landing site of the Chang'E-4 mission. *Planetary and Space Science*, 179, 104741. <https://doi.org/10.1016/j.pss.2019.104741>
- Losiak, A., Wilhelms, D. E., Byrne, C. J., Thaisen, K., Weider, S. Z., Kohout, T., & Kring, D. A. (2009). A new lunar impact crater database. In *Lunar and planetary science conference*.
- Lu, Y., Wu, Y., Michael, G. G., Ma, J., Cai, W., & Qin, N. (2021). Chronological sequence of chang'e-4 landing zone within von kármán crater. *Icarus*, 354, 114086. <https://doi.org/10.1016/j.icarus.2020.114086>
- Lucey, P. G. (2004). Mineral maps of the moon. *Geophysical Research Letters*, 31(8), L08701. <https://doi.org/10.1029/2003gl019406>
- Lucey, P. G., Taylor, G. J., Hawke, B. R., & Spudis, P. D. (1998). Feo and tio2 concentrations in the South Pole-Aitken basin: Implications for mantle composition and basin formation. *Journal of Geophysical Research*, 103(E2), 3701–3708. <https://doi.org/10.1029/97je03146>
- Matsunaga, T., Ohtake, M., Haruyama, J., Ogawa, Y., Nakamura, R., Yokota, Y., et al. (2008). Discoveries on the lithology of lunar crater central peaks. *Geophysical Research Letters*, 35, L23201. <https://doi.org/10.1029/2008gl035868>
- McKay, D. S., Heiken, G., Basu, A., Blanford, G., Simon, S., Reedy, R., & Papike, J. (1991). Physical properties of the lunar surface. In *Lunar sourcebook* (pp. 522–530).
- Meles, G. A., Van der Kruk, J., Greenhalgh, S. A., Ernst, J. R., Maurer, H., & Green, A. G. (2010). A new vector waveform inversion algorithm for simultaneous updating of conductivity and permittivity parameters from combination crosshole/borehole-to-surface GPR data. *IEEE Transactions on Geoscience and Remote Sensing*, 48(9), 3391–3407. <https://doi.org/10.1109/tgrs.2010.2046670>
- Melosh, H., Kendall, J., Horgan, B., Johnson, B., Bowling, T., Lucey, P., & Taylor, G. (2017). South Pole-Aitken basin ejecta reveal the Moon's upper mantle. *Geology*, 45(12), 1063–1066. <https://doi.org/10.1130/g39375.1>
- Mertens, L., Persico, R., Matera, L., & Lambot, S. (2016). Automated detection of reflection hyperbolas in complex GPR images with no a priori knowledge on the medium. *IEEE Transactions on Geoscience and Remote Sensing*, 54(1), 580–596. <https://doi.org/10.1109/tgrs.2015.2462727>
- Moriarty, D. P., III, & Pieters, C. M. (2015). The nature and origin of mafic mound in the South Pole-Aitken basin. *Geophysical Research Letters*, 42(19), 7907–7915. <https://doi.org/10.1002/2015gl065718>
- Moriarty, D. P., III, Watkins, R. N., Valencia, S. N., Kendall, J. D., Evans, A. J., Dygert, N., & Petro, N. E. (2021). Evidence for a stratified upper mantle preserved within the South Pole-Aitken basin. *Journal of Geophysical Research: Planets*, 126(1), e2020JE006589. <https://doi.org/10.1029/2020je006589>
- Moriarty, D. P., & Pieters, C. M. (2018). The character of South Pole-Aitken Basin: Patterns of surface and subsurface composition. *Journal of Geophysical Research: Planets*, 123, 729–747. <https://doi.org/10.1002/2017je005364>
- Moriarty, D. P., Pieters, C. M., & Isaacson, P. J. (2013). Compositional heterogeneity of central peaks within the South Pole-Aitken Basin. *Journal of Geophysical Research: Planets*, 118, 2310–2322. <https://doi.org/10.1002/2013je004376>
- Moriarty, D. P., Pieters, C. M., Nettles, J., Isaacson, P. J., Cheek, L., Head, J. W., & Petro, N. (2011). Finsen and alder: A compositional study of lunar central peak craters in the South Pole-Aitken basin. In *Lunar and planetary science conference*.
- Nakamura, R., Matsunaga, T., Ogawa, Y., Yamamoto, S., Hiroi, T., Saiki, K., & Yokota, Y. (2009). Ultramafic impact melt sheet beneath the South Pole-Aitken basin on the moon. *Geophysical Research Letters*, 36(22), L22202. <https://doi.org/10.1029/2009gl040765>
- Nash, D. B., & Conel, J. E. (1973). Vitrification darkening of rock powders: Implications for optical properties of the lunar surface. *The Moon*, 8(3), 346–364. <https://doi.org/10.1007/bf00581729>
- Oberbeck, V. R., & Quaide, W. L. (1968). Genetic implications of lunar regolith thickness variations. *Icarus*, 9(1), 446–465. [https://doi.org/10.1016/0019-1035\(68\)90039-0](https://doi.org/10.1016/0019-1035(68)90039-0)
- Olhoeft, G. R., & Strangway, D. W. (1975). Dielectric properties of the first 100 meters of the moon. In *Lunar sourcebook* (Vol. 24). [https://doi.org/10.1016/0012-821x\(75\)90146-6](https://doi.org/10.1016/0012-821x(75)90146-6)
- Paskert, J. H., Hiesinger, H., & van der Bogert, C. H. (2018). Lunar far side volcanism in and around the South Pole-Aitken basin. *Icarus*, 299, 538–562.
- Peplinski, N. R., Ulaby, F. T., & Dobson, M. C. (1995). Dielectric properties of soils in the 0.3-1.3-ghz range. *IEEE Transactions on Geoscience and Remote Sensing*, 33(3), 803–807. <https://doi.org/10.1109/36.387598>
- Pieters, C. M., & Noble, S. K. (2016). Space weathering on airless bodies. *Journal of Geophysical Research: Planets*, 121(10), 1865–1884. <https://doi.org/10.1002/2016je005128>
- Potter, R. W. K., Collins, G. S., Kiefer, W. S., McGovern, P. J., & Kring, D. A. (2012). Constraining the size of the South Pole-Aitken basin impact. *Icarus*, 220, 730–743. <https://doi.org/10.1016/j.icarus.2012.05.032>
- Qiao, L., Ling, Z., Fu, X., & Li, B. (2019). Geological characterization of the chang'e-4 landing area on the lunar farside. *Icarus*, 333, 37–51. <https://doi.org/10.1016/j.icarus.2019.05.029>
- Quaide, W., & Oberbeck, V. (1975). Development of the mare regolith: Some model considerations. *The Moon*, 13(1), 27–55. <https://doi.org/10.1007/bf00567506>
- Quaide William, L., & Oberbeck, V. R. (1968). Thickness determinations of the lunar surface layer from lunar impact craters. *Journal of Geophysical Research*, 73(16), 5247–5270. <https://doi.org/10.1029/jb073i016p05247>
- Schultz, P. H., & Crawford, D. A. (2011). Origin of nearside structural and geochemical anomalies on the Moon. In *Recent Advances and Current Research Issues in Lunar Stratigraphy*.
- Shkuratov, Y. G., & Bondarenko, N. Y. (2001). Regolith layer thickness mapping of the Moon by radar and optical data. *Icarus*, 149, 329–338. <https://doi.org/10.1006/icar.2000.6545>
- Snyder, G. A., Taylor, L. A., & Neal, C. R. (1992). A chemical model for generating the sources of mare basalts: Combined equilibrium and fractional crystallization of the lunar magmasphere. *Geochimica et Cosmochimica Acta*, 56(10), 3809–3823. [https://doi.org/10.1016/0016-7037\(92\)90172-f](https://doi.org/10.1016/0016-7037(92)90172-f)
- Stopar, J. D., Robinson, M. S., Barnouin, O. S., McEwen, A. S., Speyerer, E. J., Henriksen, M. R., & Sutton, S. S. (2017). Relative depths of simple craters and the nature of the lunar regolith. *Icarus*, 298, 34–48. <https://doi.org/10.1016/j.icarus.2017.05.022>
- Taflove, A., & Hagness, S. C. (2000). *Computational electrodynamics: The finite-difference time-domain method*. Norwood, MA, USA: Artech House.
- Tang, Z., Liu, J., Wang, X., Ren, X., Chen, W., Yan, W., et al. (2020). Physical and mechanical characteristics of lunar soil at the Chang'E-4 landing site. *Geophysical Research Letters*, 47, e2020GL089499. <https://doi.org/10.1029/2020gl089499>
- Tompkins, S., & Pieters, C. M. (1999). Mineralogy of the lunar crust: Results from Clementine. *Meteoritics & Planetary Science*, 34, 25–41. <https://doi.org/10.1111/j.1945-5100.1999.tb01729.x>

- Uemoto, K., Ohtake, M., Haruyama, J., Matsunaga, T., Yamamoto, S., Nakamura, R., et al. (2017). Evidence of impact melt sheet differentiation of the lunar South Pole-Aitken basin. *Journal of Geophysical Research: Planets*, *122*(8), 1672–1686. <https://doi.org/10.1002/2016je005209>
- Vaughan, W. M., & Head, J. W. (2014). Impact melt differentiation in the South Pole-Aitken basin: Some observations and speculations. *Planetary and Space Science*, *91*, 101–106. <https://doi.org/10.1016/j.pss.2013.11.010>
- Wai-Lok Lai, W., Dérobert, X., & Annan, P. (2018). A review of ground penetrating radar application in civil engineering: A 30-year journey from locating and testing to imaging and diagnosis. *NDT & E International*, *96*, 58–78. <https://doi.org/10.1016/j.ndteint.2017.04.002>
- Warren, C., Giannopoulos, A., & Giannakis, I. (2016). gprMax: Open source software to simulate electromagnetic wave propagation for ground penetrating radar. *Computer Physics Communications*, *209*, 163–170. <https://doi.org/10.1016/j.cpc.2016.08.020>
- Warren, C., Giannopoulos, A., Gray, A., Giannakis, I., Patterson, A., Wetter, L., & Hamrah, A. (2019). A CUDA-based GPU engine for gprMax: Open source FDTD electromagnetic simulation software. *Computer Physics Communications*, *237*, 208–218. <https://doi.org/10.1016/j.cpc.2018.11.007>
- Weiren, W., Chunlai, L., Wei, Z., Hongbo, Z., Jianjun, L., Weibin, W., & Ziyuan, O. (2019). Lunar farside to be explored by chang'e-4. *Nature Geoscience*, *12*(7), 222–223.
- Wieczorek, M. A., Neumann, G. A., Nimmo, F., Kiefer, W. S., Taylor, G. J., Melosh, H. J., et al. (2013). The crust of the Moon as seen by GRAIL. *Science*, *339*, 671–675. <https://doi.org/10.1126/science.1231530>
- Wieczorek, M. A., & Phillips, R. J. (1999). Lunar multiring basins and the cratering process. *Icarus*, *139*(2), 246–259. <https://doi.org/10.1006/icar.1999.6102>
- Wilhelms, D. E., & McCauley, J. F. (1987). *The geologic history of the moon*.
- Williams, R. M., Ray, L. E., Lever, J. H., & Burzynski, A. M. (2014). Crevasse detection in ice sheets using ground penetrating radar and machine learning. *IEEE Journal of Selected Topics in Applied Earth Observations and Remote Sensing*, *7*(12), 4836–4848. <https://doi.org/10.1109/jstars.2014.2332872>
- Xiao, Z., Ding, C., Xie, M., Cai, Y., Cui, J., Zhang, K., & Wang, J. (2021). Ejecta from the orientale basin at the chang'e-4 landing site. *Geophysical Research Letters*, *48*, e2020GL090935. <https://doi.org/10.1029/2020GL090935>
- Yamamoto, S. R., Nakamura, R., Matsunaga, T., Ogawa, Y., Ishihara, Y., Morota, T., et al. (2010). Possible mantle origin of olivine around lunar impact basins detected by SELENE. *Nature Geosciences*, *3*, 533–536. <https://doi.org/10.1038/ngeo897>
- Yee, K. (1966). Numerical solution of initial boundary value problems involving Maxwell's equations in isotropic media. *IEEE Transactions on Antennas and Propagation*, *14*(3), 302–307. <https://doi.org/10.1109/tap.1966.1138693>
- Yelf, R. (2004). Where is true time zero? In *Proceedings of the tenth international conference on grounds penetrating radar, 2004. GPR 2004* (Vol. 1, pp. 279–282).
- Yingst, R. A., Chuang, F. C., Berman, D. C., & Mest, S. C. (2017). Geologic mapping of the planck quadrangle of the moon. In *Lunar and planetary science conference*.
- Yuan, Y., Zhu, P., Zhao, N., Xiao, L., Garnero, E., Xiao, Z., et al. (2017). The 3-d geological model around chang'e-3 landing site based on lunar penetrating radar channel 1 data. *Geophysical Research Letters*, *44*(13), 6553–6561. <https://doi.org/10.1002/2017gl073589>
- Yue, Z., Yang, M., Jia, M., Michael, G., Di, K., Gou, S., & Liu, J. (2020). Refined model age for orientale basin derived from zonal crater dating of its ejecta. *Icarus*, *346*, 113804. <https://doi.org/10.1016/j.icarus.2020.113804>
- Zhang, L., Li, J., Zeng, Z., Xu, Y., Liu, C., & Chen, S. (2020). Stratigraphy of the Von Kármán crater based on Chang'E-4 lunar penetrating radar data. *Geophysical Research Letters*, *47*, e2020GL088680. <https://doi.org/10.1029/2020gl088680>
- Zheng, Y., Wang, S., Feng, J., Ouyang, Z., & Li, X. (2005). Measurement of the complex permittivity of dry rocks and minerals: Application of polythene dilution method and Lichtenecker's mixture formulae. *Geophysical Journal International*, *163*(3), 1195–1202. <https://doi.org/10.1111/j.1365-246x.2005.02718.x>
- Zongcheng, L., Bradley, L. J., Alian, W., Chunlai, L., Jianzhong, L., Jiang, Z., et al. (2015). Correlated compositional and mineralogical investigations at the Chang'e-3 landing site. *Nature Communication*, *6*, 880.